BMC Cancer

RESEARCH

Open Access

Machine learning-assisted radiogenomic analysis for miR-15a expression prediction in renal cell carcinoma

Yulian Mytsyk[1,2*], Paweł Kowal[3], Yuriy Kobilnyk[4], Mateusz Lesny[4], Michał Skrzypczyk[5], Dmytro Stroj[6], Victor Dosenko[6] and Olena Kucheruk[7]

Abstract

Background Renal cell carcinoma (RCC) is a prevalent malignancy with highly variable outcomes. MicroRNA-15a (miR-15a) has emerged as a promising prognostic biomarker in RCC, linked to angiogenesis, apoptosis, and proliferation. Radiogenomics integrates radiological features with molecular data to non-invasively predict biomarkers, offering valuable insights for precision medicine. This study aimed to develop a machine learning-assisted radiogenomic model to predict miR-15a expression in RCC.

Methods A retrospective analysis was conducted on 64 RCC patients who underwent preoperative multiphase contrast-enhanced CT or MRI. Radiological features, including tumor size, necrosis, and nodular enhancement, were evaluated. MiR-15a expression was quantified using real-time qPCR from archived tissue samples. Polynomial regression and Random Forest models were employed for prediction, and hierarchical clustering with K-means analysis was used for phenotypic stratification. Statistical significance was assessed using non-parametric tests and machine learning performance metrics.

Results Tumor size was the strongest radiological predictor of miR-15a expression (adjusted $R^2 = 0.8281$, $p < 0.001$). High miR-15a levels correlated with aggressive features, including necrosis and nodular enhancement ($p < 0.05$), while lower levels were associated with cystic components and macroscopic fat. The Random Forest regression model explained 65.8% of the variance in miR-15a expression ($R^2 = 0.658$). For classification, the Random Forest classifier demonstrated exceptional performance, achieving an AUC of 1.0, a precision of 1.0, a recall of 0.9, and an F1-score of 0.95. Hierarchical clustering effectively segregated tumors into aggressive and indolent phenotypes, consistent with clinical expectations.

Conclusions Radiogenomic analysis using machine learning provides a robust, non-invasive approach to predicting miR-15a expression, enabling enhanced tumor stratification and personalized RCC management. These findings underscore the clinical utility of integrating radiological and molecular data, paving the way for broader adoption of precision medicine in oncology.

Keywords Renal cell carcinoma, MicroRNA-15a, Radiogenomics, Machine learning, Biomarkers, Imaging features, Predictive modeling, Personalized medicine

*Correspondence:
Yulian Mytsyk
mytsyk.yulian@gmail.com
Full list of author information is available at the end of the article

Background

Renal cell carcinoma (RCC) is one of the most common malignancies of the urinary system in adults and is associated with a substantial mortality rate worldwide [1]. Despite advances in surgical, targeted, and immunotherapeutic approaches, clinical outcomes in RCC continue to vary widely [2, 3]. Precision medicine aims to tailor treatment strategies for individual patients by integrating clinical, laboratory, and molecular-genetic information, making it particularly relevant for prognostic assessment [4–6]. Accurate survival prediction in RCC patients using reliable biomarkers not only facilitates optimal therapeutic decision-making but also enhances long-term outcomes [1, 7]. Consequently, identifying novel and clinically relevant prognostic factors is crucial for improving management strategies in RCC [8].

MicroRNAs (miRNAs) are small non-coding ribonucleic acid (RNA) molecules that play a crucial role in post-transcriptional gene regulation and contribute significantly to the initiation and progression of various cancers, including RCC [9–11]. Mounting evidence indicates that aberrant miRNA expression not only influences tumorigenesis and metastatic dissemination but also represents a promising diagnostic and prognostic biomarker [12, 13]. Among these, miR-15a has garnered particular attention for its involvement in key oncogenic pathways, including angiogenesis, proliferation, and apoptosis [14–19]. MiR-15a is encoded by a gene on chromosome 13q14.3. Its downregulation has been observed in multiple malignancies, including prostate cancer, chronic lymphocytic leukemia, nasopharyngeal carcinoma, malignant melanoma, glioma, and breast cancer, indicating a tumor-suppressive role. By targeting several oncogenes, such as B-cell lymphoma 2 (BCL2), myeloid cell leukemia 1 (MCL1), cyclin D1 (CCND1), and Wnt family member 3A (WNT3A), miR-15a promotes apoptosis and restricts cellular proliferation, thereby contributing to tumor suppression [20–22].

Numerous studies have highlighted the diagnostic and prognostic significance of miR-15a in RCC, linking its dysregulated expression to more aggressive disease characteristics, increased metastatic potential, and reduced overall survival (OS) [23–25]. This may be attributed to the regulation of pri-miR-15a nuclear binding by protein kinase Cα (PKCα), which plays a critical role in endothelin-1 (ET-1)-mediated signaling—a pathway known to contribute to tumor progression. ET-1 signaling is involved in key processes such as tumor angiogenesis, proliferation, and metastasis, and may therefore play a significant role in RCC pathogenesis [26, 27]. In addition, miR-15a is involved in the noncanonical nuclear factor kappa B (NF-κB) pathway, which regulates apoptosis resistance, angiogenesis, and multidrug resistance. Meanwhile, the von Hippel–Lindau (VHL) gene functions as a negative regulator of NF-κB [28, 29]. Previously, we reported that miR-15a detected in urine samples could serve as a non-invasive diagnostic biomarker for RCC [30], whereas its tissue expression was identified as a significant prognostic marker for OS in clear cell RCC (ccRCC) [31]. This body of evidence highlights the significance of miR-15a as a biomarker for both risk stratification and potential targeted therapies. Evaluating miR-15a expression levels may provide valuable insights for improved patient stratification and the development of personalized treatment strategies [10, 32–35].

However, in real-world clinical settings, comprehensive molecular-genetic analyses are not always feasible, posing limitations to the use of microRNAs as biomarkers. With advancements in modern imaging modalities and high-throughput molecular assays, radiogenomics has emerged as an innovative approach that integrates radiological features with genomic and transcriptomic data [5, 36]. This non-invasive approach allows clinicians and researchers to correlate specific imaging phenotypes (e.g., from MRI or CT) with distinct gene and miRNA expression profiles, providing valuable insights into intratumoral heterogeneity [37–39]. Radiogenomic models hold significant potential for reliably predicting microRNA expression, which, in turn, may enhance risk stratification and support more personalized treatment strategies for RCC patients [40]. In the context of RCC, radiogenomic analysis has the potential to predict the expression of key molecular markers, such as miR-15a, reducing the need for tissue biopsies and advancing the goals of precision medicine [41–43]. Moreover, the personalization of RCC management through molecular and imaging-based biomarkers continues to evolve, reflecting a broader shift toward individualized therapeutic decision-making.

Material and methods

Aim

This study aimed to develop and validate a radiogenomic approach, assisted by machine learning, for the non-invasive prediction of miR-15a tissue expression in RCC.

Compliance with ethical standards

This retrospective study was approved by the Bioethical Committee of Danylo Halytsky Lviv National Medical University (protocol #5, dated 25.05.2015). All procedures adhered to the ethical guidelines established by institutional and national research committees, in accordance with the principles of the 1964 Helsinki Declaration and its later amendments or equivalent ethical standards. The study was conducted between 2015 and

2024. Written informed consent was obtained from all patients prior to inclusion in the study.

Study design

This study employed a machine learning-assisted radiogenomic strategy to predict miR-15a expression in RCC. Radiological features derived from preoperative imaging were integrated with molecular data and analyzed via Random Forest and polynomial regression models. By correlating these imaging-based predictors with miR-15a expression, we aimed to establish a non-invasive framework for enhanced tumor stratification and personalized RCC management. The overall study workflow is depicted in Fig. 1.

Characteristics of participants

After a careful retrospective selection from the archived medical records of 286 RCC patients, 64 cases were included in the analysis. The inclusion criteria were as follows: adult patients with a pathologically confirmed clear cell RCC (ccRCC) subtype; surgical treatment performed as either partial nephrectomy (n = 14; 21.88%) or radical nephrectomy (n = 50; 78.12%); and preoperative abdominal multiphase contrast-enhanced computed tomography (MCECT) and/or contrast-enhanced MRI with satisfactory image quality. The exclusion criteria included non-ccRCC histology, a history of preoperative treatment for RCC, absence of a postoperative pathological report, and/or unavailability of formalin-fixed paraffin-embedded (FFPE) tissue specimens containing preserved RCC samples for analysis.

The gender distribution was as follows: 37 men (57.81%) and 27 women (42.19%). Patients' ages ranged from 47 to 68 years, with a mean age of 61.2 ± 6.33 years. Tumor sizes ranged from 3.2 to 11.8 cm, with an average of 8.52 ± 3.59 cm. No cases of distant metastasis were observed. Staging was performed according to the American Joint Committee on Cancer (AJCC) Tumor, Node, Metastasis (TNM) classification, while pathological classification followed the World Health Organization (WHO) system. Tumor grading was assessed using the International Society of Urological Pathology (ISUP) grading system, which categorizes RCC into four prognostic grades based on histological features. A detailed clinical analysis of the patients is presented in Table 1.

miRNA isolation from paraffin-embedded tissue

To investigate miR-15a expression in RCC tissues, FFPE specimens containing postoperatively preserved RCC samples were retrieved from archives. Tissue samples were deparaffinized, and RNA was isolated using the PureLink™ FFPE RNA Isolation Kit (Applied Biosystems, USA) following the manufacturer's protocol. RNA concentration was measured using a NanoDrop ND1000 spectrophotometer (NanoDrop Technologies Inc., USA).

qPCR data

The expression of miR-15a was quantified using reverse transcription followed by real-time quantitative polymerase chain reaction (qPCR). Reverse transcription was performed using the TaqMan™ MicroRNA Reverse Transcription Kit (Applied Biosystems, USA) with a specific primer for miR-15a and 10 ng of total RNA. Real-time

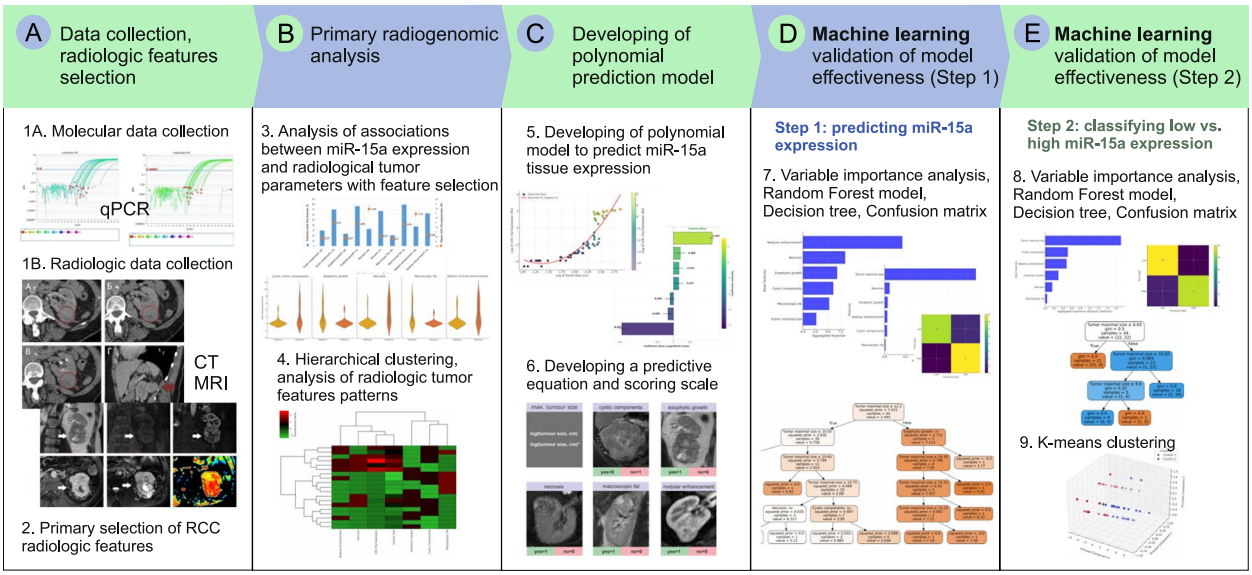

Fig. 1 The figure depicts the workflow of the study

Table 1 Clinical characteristics of the patients

Subgroup	N	Mean Age, years	Age Std Dev, years	Mean Tumor Size, cm	Tumor Size Std Dev, cm	Percentage
Gender						
Male	37	64.27	5.86	4.88	3.77	57.81
Female	27	47.12	6.25	11.07	3.3	42.19
Tumour site						
Right	30	56.94	7.42	7.25	4.29	46.88
Left	34	64.06	5.25	4.03	3.62	53.12
Stage						
T1aN0	13	49.45	7.55	4.2	2.61	20.31
T1bN0	10	57.81	7.53	5.14	3.64	15.62
T2aN0	16	57.32	6.6	6.09	3.96	25.0
T2bN0	8	57.58	7.57	7.03	2.75	12.5
T3aN0	9	48.08	5.13	7.97	2.71	14.06
T3aN1	2	61.39	6.37	8.91	3.9	3.12
T3bN0	1	50.25	7.37	9.86	2.72	1.56
T3bN1	5	58.29	6.78	10.8	3.78	7.81
ISUP Grade						
ISUP Grade 1	15	60.35	5.95	9.79	3.29	23.44
ISUP Grade 2	14	64.79	5.32	9.48	4.27	21.88
ISUP Grade 3	22	65.22	6.01	10.31	3.03	34.38
ISUP Grade 4	13	53.98	6.24	11.1	3.73	20.31

ISUP The International Society of Urological Pathology, *Std Dev* Standard deviation

qPCR was conducted using TaqMan™ MicroRNA Assays (Applied Biosystems, USA), with U6 snRNA (ID 001973) as an endogenous control and hsa-miR-15a (ID 000389) as the target miRNA.

The thermal cycling conditions were as follows: initial denaturation at 95 °C for 10 min, followed by 50 cycles of 95 °C for 15 s and 60 °C for 60 s. Expression levels of miRNA were normalized to U6 snRNA and expressed in relative units (RU), which represent the relative quantification of miR-15a expression using the ΔΔCt method in qPCR analysis. Amplifications were performed on a 7500 Fast Real-Time PCR system (Applied Biosystems, USA), and results were analyzed using the 7500 Fast Real-Time PCR software package.

CT examination

An abdominal MCECT was performed using a BrightSpeed 16 multislice CT scanner (General Electric®, USA). Scans were acquired with the patient in the supine position using a spiral acquisition method in the craniocaudal direction. To minimize motion artifacts, patients were instructed to hold their breath during the scans. The scanning protocol followed the manufacturer's guidelines with the following parameters: spiral density = 5.0 mm, pitch = 1.375:1, speed = 27.50 mm/rotation, interval = 5.0 mm, gantry tilt angle = 80.0°, FOV = 46 × 46 cm, kV = 130, mA = 350, and total radiation dose = 20–30 mSv. The total examination time ranged from 10 to 20 min.

MCECT imaging was performed in four phases: non-contrast phase (NCP), corticomedullary phase (CMP), nephrographic phase (NP), and excretory phase (EP). CMP, characterized by bright enhancement of the renal cortex with minimal enhancement of the medulla, was captured 35–40 s after contrast injection. NP, defined by homogeneous enhancement of both the cortex and medulla without contrast excretion into the collecting system, was performed with a delay of 70–75 s. EP, marked by contrast excretion into the collecting system, was obtained after 8–10 min. The contrast medium, either iopromide or iohexol, was administered intravenously at 1–1.2 mL per kg of body weight through an 18-gauge needle inserted into the antecubital vein. The injection was delivered at a flow rate of 3 mL/s using a semi-automated power injector (Dual Shot alpha 7, Nemoto®, Japan), followed by 40 mL of saline. No adverse reactions to the contrast medium were observed. To prepare for the examination, patients fasted and consumed 1.5 L of fluid beforehand.

MRI protocol

An abdominal contrast-enhanced MRI was performed according to a standardized protocol using a 1.5 T body scanner (Signa HDxt, General Electric, USA) with an eight-channel phased-array body coil. The imaging protocol included the following sequences and parameters:

1. Coronal T2-weighted Single-Shot Fast Spin Echo (SSFSE): TR = 2625 ms, TE = 90 ms, flip angle = 90°, field of view (FOV) = 40 × 40 cm, matrix = 200 × 192, breath-hold. Provides essential T2-weighted anatomical information.
2. Axial 2D Fat-Saturated Fast Imaging Employing Steady-State Acquisition (FIESTA FAT SAT): TR = 4.1 ms, TE = 1.8 ms, flip angle = 90°, FOV = 40 × 40 cm, matrix = 224 × 320. An ultrafast pulse sequence that generates high-resolution images with excellent contrast and a high signal-to-noise ratio (SNR). Compared to other steady-state pulse sequences, FIESTA minimizes signal saturation and motion artifacts, offering superior image quality.
3. Axial Diffusion-Weighted Imaging (DWI): TR = 12,000 ms, TE = 90 ms, FOV = 40 × 40 cm, matrix = 200 × 192, number of excitations (NEX) = 3, bandwidth = 250 kHz, diffusion direction = slice, slice thickness = 6 mm, interscan gap = 1 mm, b-values = 0 and 600 s/mm^2, acquisition time = 17 s. Conducted before contrast administration using a single-shot echo-planar imaging sequence with parallel imaging and fat saturation, performed during a single breath-hold.
4. Axial T1-weighted Fast Spoiled Gradient-Recalled-Echo Dual Echo (FSPGR-DE): TR = 130 ms, TE = 2.1 ms and 4.3 ms, flip angle = 70°, FOV = 43 × 43 cm, matrix = 320 × 192, breath-hold.
5. Axial T2-weighted Fast Recovery Fast Spin Echo (FRFSE): TR = 8750 ms, TE = 78 ms and 132 ms, flip angle = 90°, FOV = 44 × 44 cm, matrix = 384 × 192.
6. Sagittal T2-weighted SSFSE: TR = 1760 ms, TE = 87.4 ms, flip angle = 90°, FOV = 37 × 37 cm, matrix = 384 × 256.
7. Axial 3D Fat-Saturated T1-weighted Spoiled Gradient Echo (LAVA): TR = 4.5 ms, TE = 2.2 ms, flip angle = 15°, FOV = 38 × 38 cm, matrix = 320 × 192. This sequence was conducted during and after the administration of gadopentetate dimeglumine at a dose of 0.1 mmol/kg body weight as a bolus injection. Imaging was performed with 20-s intervals between each breath-hold acquisition. The protocol combines contrast-enhanced multiphase imaging with high resolution, large coverage, and uniform fat suppression. LAVA acquires thin, overlapping slices in a single breath-hold, providing high in-plane resolution. Multiple acquisitions were obtained to capture arterial and venous phases, enabling detailed anatomical and vascular assessment. Maximum intensity projection (MIP) post-processing further enhanced vascular visualization.

Image analysis and selection of RCC radiologic features

Preoperative imaging was performed using CT in 41 cases (64.06%) and MRI in 23 cases (35.94%). All images were transmitted to a picture archiving and communication system (PACS) for interpretation using workstations. CT and MRI image features were independently evaluated by two board-certified radiologists with extensive experience in urogenital radiology, who were blinded to miR-15a expression. For CT and MRI data processing, RadiAnt DICOM Viewer (https://www.radiantviewer.com) was used.

A detailed topographic characterization was performed for all renal lesions, including assessment of tumor maximal diameter (in centimeters) and localization by site and pole (upper, middle, or lower). Only qualitative tumor features were selected for radiomic analysis. Radiological tumor parameters were chosen based on their detectability using both contrast-enhanced CT and MRI, as well as their frequency of occurrence to allow for statistical analysis. As a result, the following imaging features were included in the analysis:

1. Morphological features:
    a) Shape: round, oval, irregular, or lobulated;
    b) Margins: well-defined, ill-defined, infiltrative, or encapsulated;
    c) Growth pattern: exophytic (≥ 50% of the tumor extending beyond the kidney contour), endophytic, mixed, or multicentric;
    d) Pseudocapsule presence: complete, incomplete, or absent;
    e) Cystic components: present or absent;
    f) Necrosis: present or absent;
    g) Calcifications: present or absent;
    h) Fat content: presence of macroscopic fat;
2. Enhancement patterns: homogeneous, nodular, rim enhancement, or septal/wall enhancement.
3. Tumor vascularity: hypervascular, hypovascular, or avascular.
4. Tumor-parenchyma interface: sharp, infiltrative, or obscured.

Primary statistical analysis

Descriptive statistics were used to summarize the patients' baseline demographic and tumor characteristics. Comparisons of categorical variables were conducted using the Pearson Chi-square test or Fisher's exact test. The normality of miR-15a expression distribution was assessed using the Shapiro–Wilk test ($W = 0.531$, $p = 0.001$). As the W-statistic was significant ($p < 0.05$), the assumption of normal data distribution was rejected. Consequently, differences between groups were evaluated using the nonparametric Mann–Whitney U test. Correlation analysis was performed using the Pearson method. A p-value of < 0.05 was considered statistically significant.

Statistical analysis was conducted to assess the relationship between miR-15a expression and radiological tumor features. For categorical variables (e.g., presence or absence of necrosis, cystic components, macroscopic fat), the Kruskal–Wallis test was used to evaluate differences in miR-15a expression across categories. Pairwise post hoc comparisons were performed using Dunn's test with Bonferroni correction to adjust for multiple comparisons. For continuous variables (e.g., tumor maximal diameter), the association between miR-15a expression and tumor size was assessed using Spearman's rank correlation coefficient due to the non-normal distribution of miR-15a expression. A linear regression analysis was performed to evaluate whether necrosis or other radiologic features confounded the relationship between tumor size and miR-15a expression.

A hierarchical clustering analysis was conducted to explore the relationships between radiologic tumor features, tumor size, and miR-15a expression levels. Data were standardized to ensure comparability across variables, and clustering was performed using Ward's method with Euclidean distance as the metric. A heatmap was generated to visualize the clustering results.

Radiogenomic analysis and machine learning

A polynomial regression model was constructed to determine the association coefficients between miR-15a expression and tumor radiological parameters, including tumor size, cystic components, exophytic growth, necrosis, macroscopic fat, and nodular enhancement. Model accuracy was assessed using the Fisher method (adjusted R^2).

To evaluate the model's effectiveness, a machine learning approach was employed. The dataset was split into a training set and a test set to assess the model's ability to generalize to new, unseen data:

- Training set (70% of the data): This portion of the data was used to train the model. The model "learned" from the training data by adjusting its parameters (e.g., coefficients in regression models) to minimize the loss function or maximize the likelihood of correct predictions.
- Test set (30% of the data): After training, the model's performance was evaluated on the test set, a portion of the data not used during training, providing an objective assessment of the model's ability to generalize to new data.

For Step 1 (predicting miR-15a expression), a Random Forest regression model was applied to evaluate the importance of radiological features, with mean squared error (MSE) used to measure model accuracy. A decision tree was also constructed for visualization.

For Step 2 (classifying low vs. high miR-15a expression), a Random Forest classifier was employed to categorize miR-15a expression as "Low" (≤ 0.10 RU) or "High" (> 0.10 RU). Model performance was assessed using precision, recall, and F1-score, while the AUC from ROC analysis was used to evaluate model discrimination. The threshold of ≤ 0.10 RU for miR-15a expression was chosen based on our previous study, which identified that miR-15a expression above this level was associated with poorer survival outcomes in ccRCC patients [31].

To assess the potential impact of a healthy control group (negative dataset) on model performance, we incorporated 15 FFPE normal renal specimens from a prior study [31]. A secondary Random Forest model was trained on the combined dataset, and performance was compared using R^2.

All models were trained and tested using a training/test split methodology to evaluate generalization. K-means clustering was applied to radiological features, including tumor size, and the data were visualized in a 3D scatter plot using principal component analysis (PCA) for dimensionality reduction.

Statistical analysis was conducted at a significance level of $p < 0.05$ using Excel v.2019, SPSS v.22, R software (v.3.3.2), and Python (SciPy library, v.1.1).

Results

Primary statistical analysis

The mean miR-15a expression in patients with RCC was 1.52 ± 2.62 RU. A significant association, determined using the Kruskal–Wallis test, was found between miR-15a tissue expression and several radiological tumor parameters: tumor maximal diameter ($p = 0.003$), cystic components ($p = 0.017$), exophytic growth ($p = 0.011$), necrosis ($p = 0.008$), macroscopic fat ($p = 0.024$), and

nodular contrast enhancement pattern ($p=0.021$). No significant correlation was observed between miR-15a expression and other radiological features ($p>0.05$). The analysis revealed that radiological features such as cystic tumor components, exophytic growth, necrosis, macroscopic fat, and nodular contrast enhancement were identified in 29.69%, 23.44%, 32.81%, 20.31%, and 37.50% of patients, respectively. Presented below is an analysis of miR-15a expression in relation to those radiologic features.

Cystic tumor components

Mean miR-15a expression was significantly lower in tumors with cystic components (0.35 ± 1.02 RU) compared to those without (2.01 ± 2.93 RU; $p<0.05$). Tumors with cystic components exhibited a narrow interquartile range (0.07 RU), indicating low variability in miR-15a expression. In contrast, tumors without cystic components displayed greater variability (IQR = 4.54 RU), suggesting heterogeneity in expression levels.

Exophytic growth

Tumors with exophytic growth had markedly lower miR-15a expression (0.34 ± 1.09 RU) compared to tumors with endophytic or mixed growth (1.88 ± 2.85 RU; $p<0.05$). The skewness (3.85) and kurtosis (14.86) values for exophytic growth indicate a strong positive skew and a leptokurtic distribution, suggesting that a few high-expression outliers contribute to increased variability.

Necrosis

Tumors with necrosis demonstrated the highest miR-15a expression (3.45 ± 3.19 RU), significantly elevated compared to tumors without necrosis (0.57 ± 1.63 RU; $p<0.05$). The wide interquartile range for tumors with necrosis (6.23 RU) reflects substantial heterogeneity in expression levels, which may correlate with diverse underlying tumor biology and progression rates.

Macroscopic fat

The lowest levels of miR-15a expression were observed in tumors with macroscopic fat (0.30 ± 0.87 RU), significantly reduced compared to those without fat components (1.83 ± 2.83 RU; $p<0.05$). Interestingly, the minimum expression value (0.01 RU) was consistent across both groups, but the maximum expression for tumors with macroscopic fat (3.18 RU) was considerably lower than for those without (9.25 RU).

Nodular contrast enhancement

Tumors with nodular enhancement showed high miR-15a expression (2.91 ± 3.24 RU) compared to tumors without this feature (0.68 ± 1.72 RU; $p<0.05$). The range of expression for tumors with nodular enhancement (9.23 RU) and its associated interquartile range (5.65 RU) underline considerable variability, potentially reflecting a link to heterogeneous vascular characteristics.

Table 2 and Fig. 2 provide a summary of miR-15a expression across different tumor radiologic features in RCC. The violin plots of miR-15a expression by radiological features are presented on Fig. 3.

A strong positive correlation was identified between the tumor size in the largest section in patients with ccRCC and the expression level of miR-15a, with a Pearson correlation coefficient of 0.724 ($p<0.001$), Fig. 4.

In a set of linear regression models (Supplementary Table S1), we examined tumor size, necrosis, cystic components, exophytic growth, macroscopic fat, and nodular enhancement in both univariate and multivariate contexts. While necrosis alone displayed a significant association with miR-15a (adjusted $R^2 \sim 0.26$, $p<0.001$), it became non-significant ($p=0.27$) and did not improve

Table 2 Summary of miR-15a expression across tumor radiologic features in RCC

Tumor Radiologic Feature	N	Mean, RU	Median, RU	Std Dev, RU	95% Confidence Interval for Mean, RU	Min., RU	Max., RU	Skewness	Kurtosis	Interquartile Range, RU
Cystic Components: Yes	19	0.35	0.04	1.02	(−0.14, 0.84)	0.01	4.27	3.65	13.77	0.07
Cystic Components: No	45	2.01	0.16	2.93	(1.13, 2.89)	0.01	9.25	1.17	−0.19	4.54
Exophytic Growth: Yes	15	0.34	0.04	1.09	(−0.26, 0.94)	0.01	4.27	3.85	14.86	0.05
Exophytic Growth: No	49	1.88	0.15	2.85	(1.06, 2.69)	0.01	9.25	1.28	0.14	3.65
Necrosis: Yes	21	3.45	2.98	3.19	(1.99, 4.90)	0.05	9.25	0.36	−1.36	6.23
Necrosis: No	43	0.57	0.04	1.63	(0.07, 1.08)	0.01	7.26	3.25	9.73	0.13
Macroscopic Fat: Yes	13	0.3	0.02	0.87	(−0.23, 0.82)	0.01	3.18	3.56	12.77	0.08
Macroscopic Fat: No	51	1.83	0.14	2.83	(1.03, 2.62)	0.01	9.25	1.31	0.21	4.13
Nodular Enhancement: Yes	24	2.91	1.1	3.24	(1.54, 4.28)	0.02	9.25	0.67	−1.15	5.65
Nodular Enhancement: No	40	0.68	0.05	1.72	(0.13, 1.23)	0.01	6.63	2.73	6.24	0.13

RU relative units, *Std Dev* Standard deviation

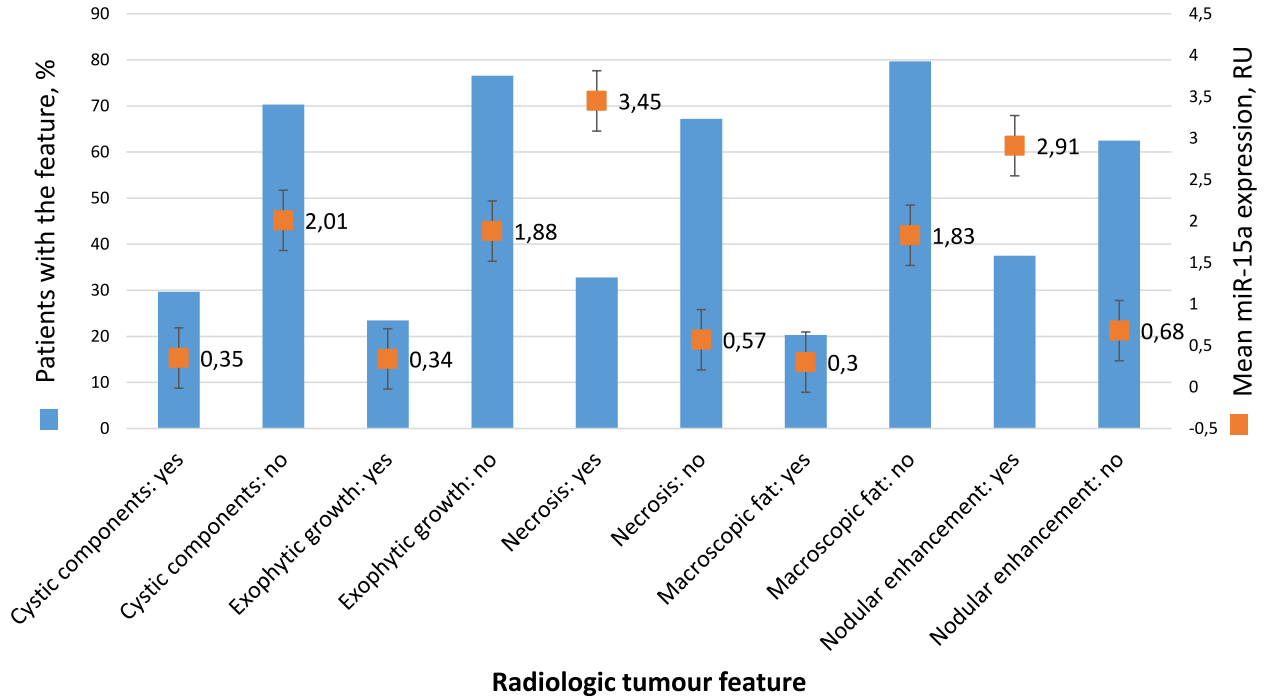

Fig. 2 Mean miR-15a levels by radiologic feature presence and their frequency. Legend: The mean levels of miR-15a expression (orange boxes, with whiskers representing the standard error) in relation to the presence or absence of radiologic features, along with their frequency (represented by columns)

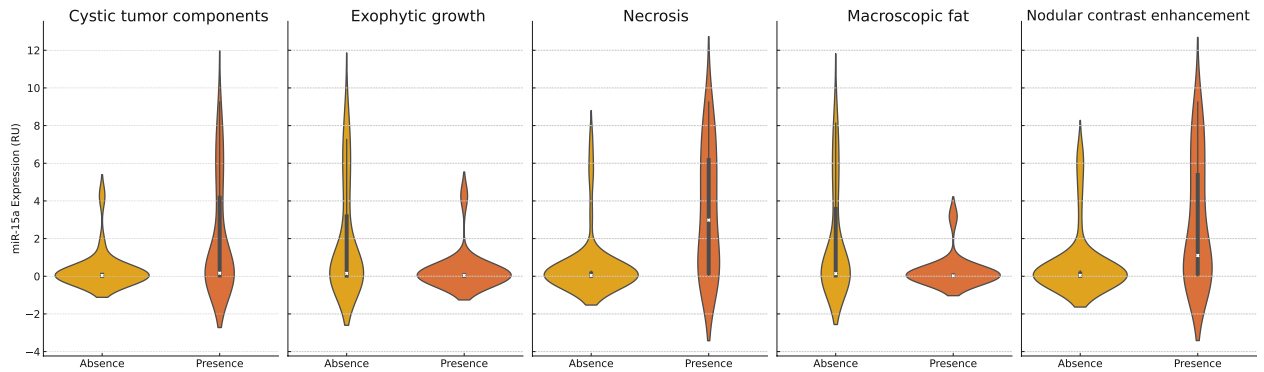

Fig. 3 The violin plots of miR-15a expression by radiological features

the adjusted R^2 (~0.50–0.52) once tumor size was included. These findings indicate that necrosis does not confound the link between tumor size and miR-15a expression.

Hierarchical clustering grouped tumors into distinct patterns based on radiologic features, tumor size, and miR-15a expression. Radiologic features, including cystic components, exophytic growth, necrosis, macroscopic fat, and nodular enhancement, formed separate clusters, while tumor size and miR-15a expression clustered independently due to their continuous variability. Larger tumors were associated with aggressive radiologic features, such as necrosis and nodular enhancement.

High miR-15a expression was predominantly observed in tumors lacking macroscopic fat and cystic components, suggesting a potential link to aggressive tumor phenotypes. In contrast, low miR-15a expression was more common in tumors with benign characteristics, such as macroscopic fat and cystic components. Notably, necrosis and nodular enhancement frequently clustered together, while cystic components showed an inverse relationship with these aggressive features. The clustering

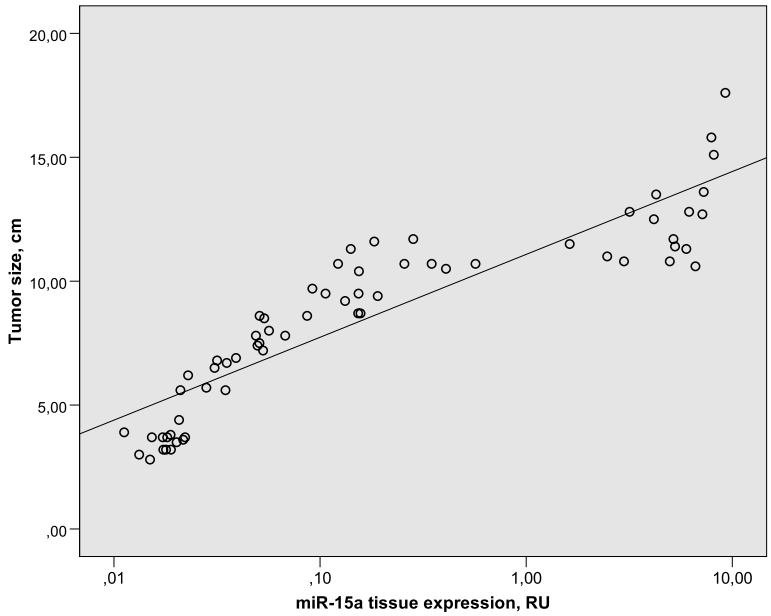

Fig. 4 Scatterplot of miR-15a levels and tumor size correlation in RCC patients

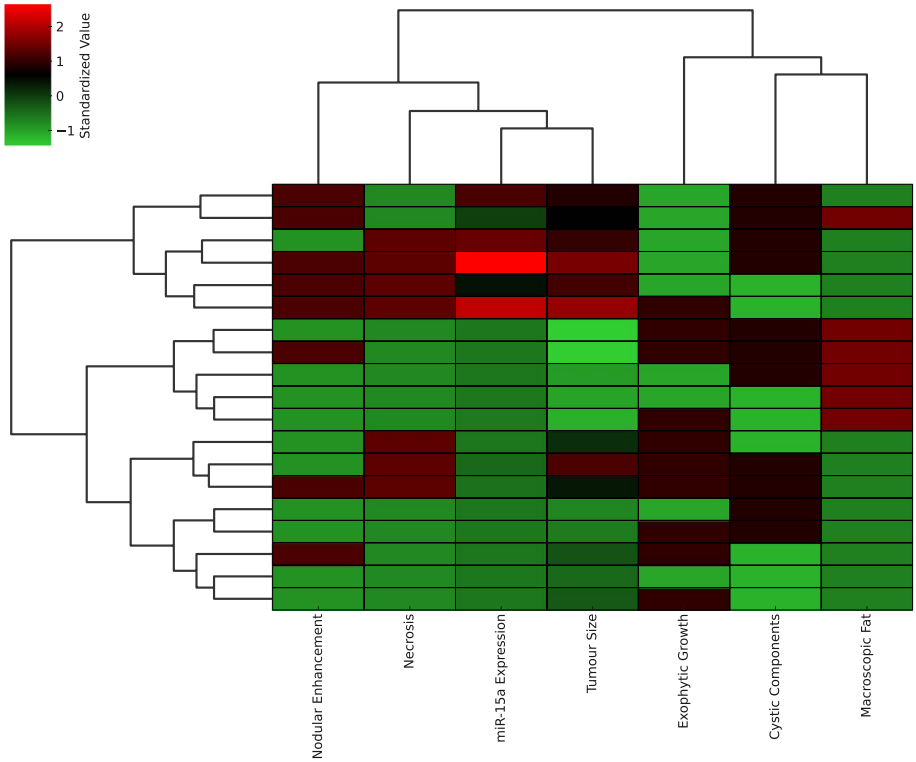

Fig. 5 Hierarchical Clustering Heatmap of Radiologic Features and miR-15a Expression

results distinctly separated tumors into aggressive versus benign phenotypic groups, aligning with clinical expectations (Fig. 5).

Machine learning-assisted radiogenomic analysis

In constructing a nonlinear regression model, tumor size was identified as the most significant predictor of miR-15a expression among radiological RCC features. When used as the sole predictor, tumor size yielded an adjusted R^2 of 0.8281 ($p < 0.001$), explaining 82.81% of the variance in miR-15a expression, Fig. 6.

The polynomial model demonstrated associations between radiologic features and the predictive outcome. Positive effects were identified for the presence of tumor necrosis (coefficient: 0.4085) and nodular contrast enhancement (coefficient: 0.3326), consistent with their established roles in tumor aggressiveness and vascularity. Negative associations were noted for the presence of exophytic growth (coefficient: −0.3382) and macroscopic fat (coefficient: −0.2048), reflecting their less invasive or indolent characteristics. The absence of cystic components (coefficient: 0.3172) was linked to more solid and potentially aggressive tumors. While individual features lacked statistical robustness, their combined effects were considered to enhance the predictive accuracy of radiogenomic model, as summarized in Table 3. Figure 7 presents a chart illustrating the regression coefficients and standard errors for radiologic characteristics used in a predictive model, demonstrating the predictors' relative importance and the model's ability to capture nonlinear relationships.

When tumor size was combined with the aforementioned radiological features to predict miR-15a tissue expression, the results improved further, yielding an adjusted R^2 of 0.8336 ($p < 0.001$). In other words, 83.36% of the variance in miR-15a expression could be accounted for by the polynomial model (degrees of freedom = 2).

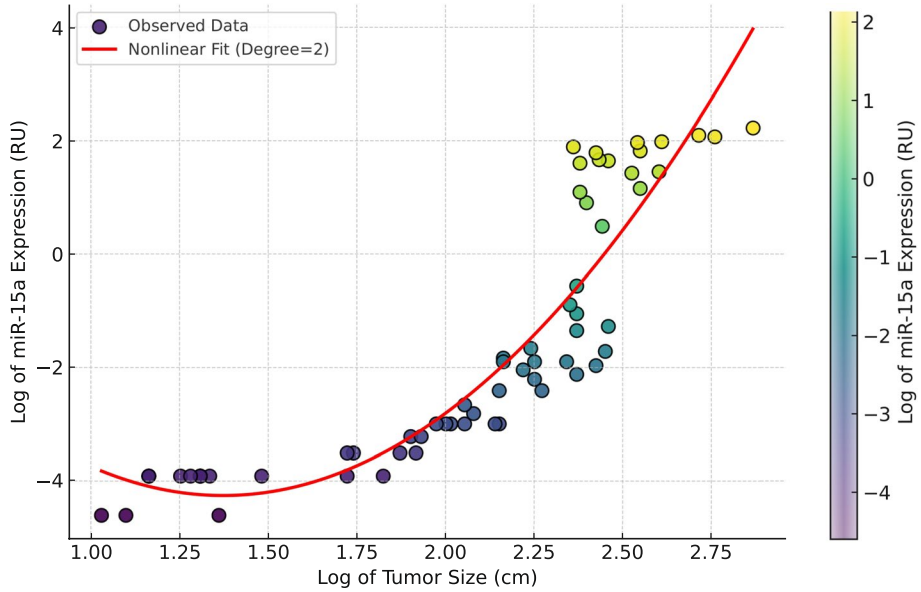

Fig. 6 Nonlinear association between log miR-15a expression and log RCC tumor size (df = 2)

Table 3 Statistical coefficients of the polynomial model predicting miR-15a expression based on RCC radiological features

Radiological characteristics of the tumor	Coefficient value	Standard error	*t*	*Pr(>|t|)*
Constant	1.5798	1.9440	0.813	0.419852
Log(Tumor Size), Degree of Freedom 1	−8.4927	2.1705	−3.913	0.000249
Log(Tumor Size), Degree of Freedom 2	3.1016	0.5923	5.236	2.55e-06
Absence of cystic tumor component	0.3172	0.2688	1.180	0.243005
Presence of exophytic growth of RCC ≥ 50% beyond the kidney contour	−0.3382	0.2849	−1.187	0.240242
Presence of tumor necrosis	0.4085	0.3242	1.260	0.212925
Presence of macroscopic fat	−0.2048	0.3150	−0.650	0.498233
Presence of nodular contrast enhancement	0.3326	0.2854	1.165	0.248904

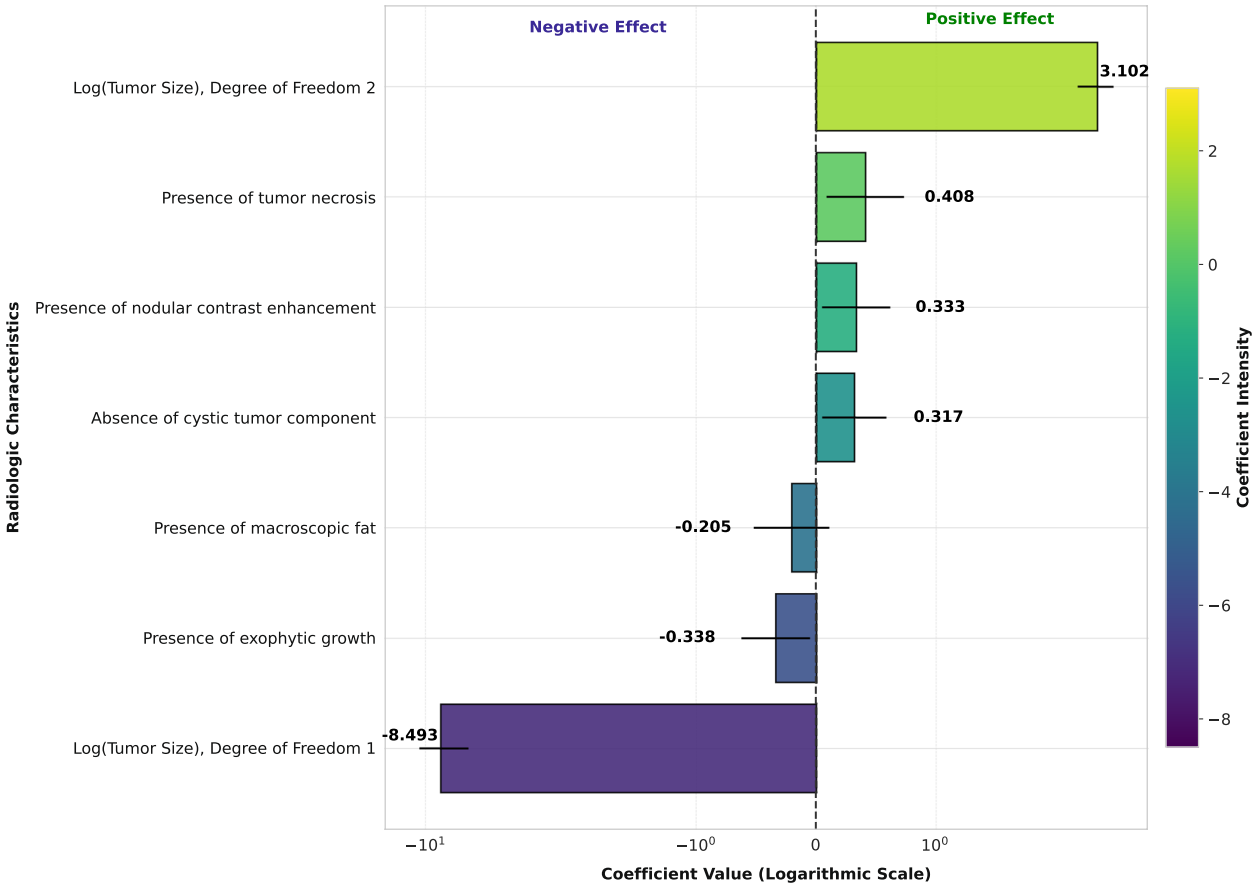

Fig. 7 Regression coefficients and standard errors for RCC radiologic characteristics in the predictive model. Legend: Visualization of regression coefficients (horizontal bars) and standard errors (whiskers) for RCC radiologic characteristics in the predictive model

A predictive equation was developed based on the obtained data to estimate the tissue expression of miR-15a using the radiological features of RCC. In the equation, the term "tumor size" should be substituted with the numerical value of the RCC size in its largest dimension (in cm). For other radiological tumor parameters, their names should be replaced with either 1 or 0, reflecting the presence or absence of the feature (as specified in parentheses), as shown in Eq. 1.

$$\begin{aligned} \boldsymbol{log(miR-15a)} &= 1.5798 - 8.4927 \times \log(\text{tumor size})\log(\text{tumor size})^2 + 0.3172 \times \text{cystic component}(\text{no}=1, \text{yes}=0) \\ &\quad - 0.3382 \times \text{exophytic growth}(\text{yes}=1, \text{no}=0) + 0.4085 \times \text{necrosis}(\text{yes}=1, \text{no}=0) \\ &\quad - 0.2048 \times \text{macroscopic fat}(\text{yes}=1,\ \text{no}=0) + 0.3326 \times \text{nodular enhancement}(\text{yes}=1, \text{no}=0) \end{aligned} \tag{1}$$

where log(miR-15a) represents the logarithm of miR-15a expression.

To facilitate the use of the developed model, we created and visualized a scoring scale for assessing the radiological parameters of RCC, assigning each parameter a corresponding coefficient, Fig. 8.

Machine learning-assisted validation of model effectiveness

Step 1: predicting miR-15a expression

The regression model, incorporating tumor size and radiological features (e.g., cystic components, exophytic growth, necrosis, macroscopic fat, and nodular enhancement), demonstrated moderate accuracy in predicting miR-15a expression as a continuous variable. Variable importance analysis using both polynomial regression and Random Forest models consistently identified nodular enhancement as the most significant predictor, followed by necrosis and tumor size (Fig. 9).

In the Random Forest model, tumor size showed a stronger direct contribution than in the polynomial regression analysis, underscoring its importance in non-linear relationships. Features such as cystic

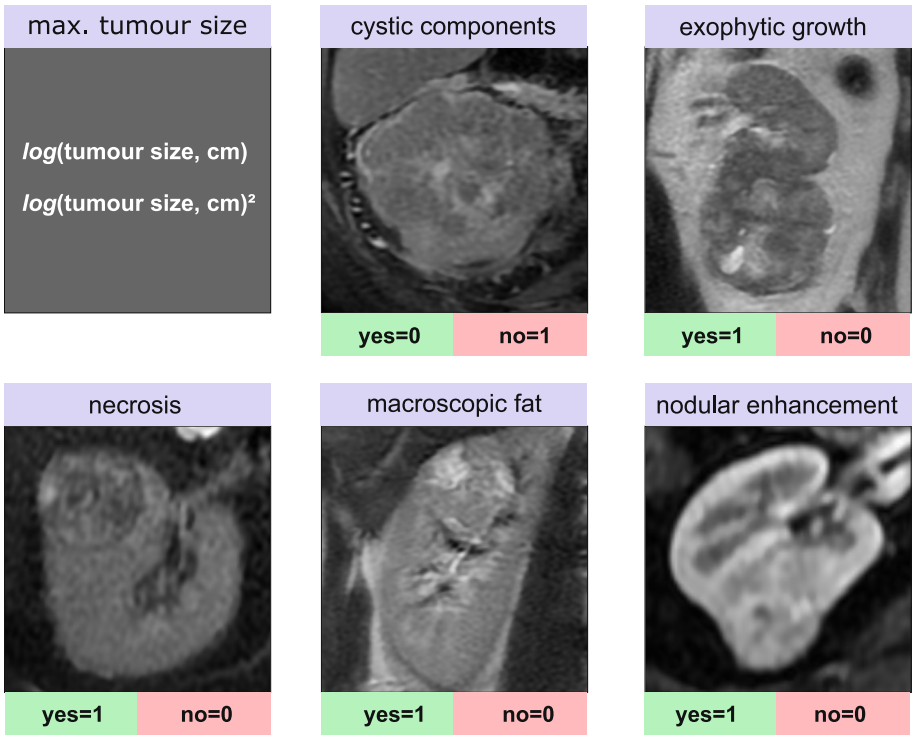

Fig. 8 Scoring scale for RCC radiological parameters predicting miR-15a expression via polynomial regression

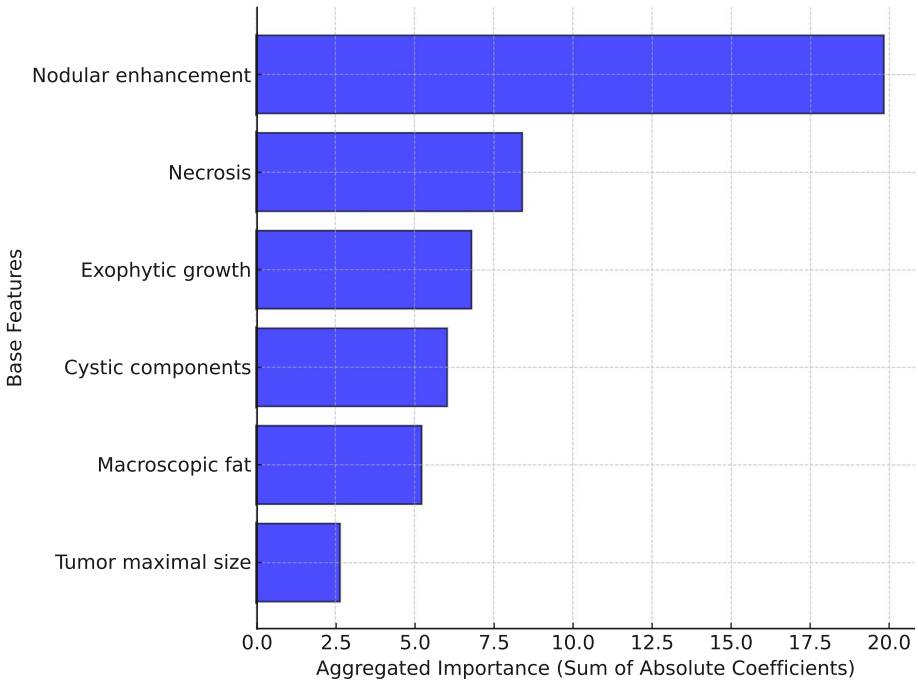

Fig. 9 Variable importance analysis for Step 1

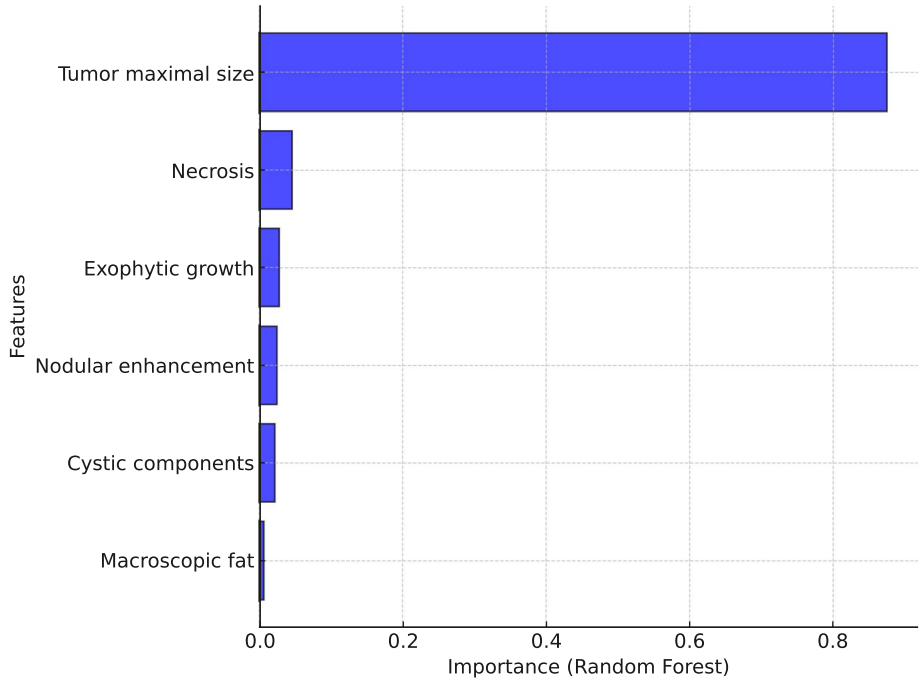

Fig. 10 Random Forest model for Step 1

components, macroscopic fat, and exophytic growth contributed less to the prediction (Fig. 10).

The model achieved an R^2 of 0.658, explaining 65.8% of the variance in miR-15a expression, with a root mean square error (RMSE) of 1.454 RU. Residual analysis revealed no systematic biases, though variability in residuals suggested reduced performance for certain samples.

In assessing whether the inclusion of a healthy control group enhances radiogenomic model performance, we observed that the R^2 coefficient notably decreased from 0.658 to −1.54, indicating reduced model explanatory power and increased variance. A statistical comparison of prediction errors between models (t-test, $p = 0.46$) confirmed that the differences were not significant. These findings suggest that adding control samples did not improve prediction accuracy and instead increased model variance.

To enhance interpretability, a decision tree was constructed to visualize the splits in the data based on feature importance. This provided an intuitive representation of how variables like nodular enhancement, necrosis, and tumor size contributed to predicting miR-15a expression (Fig. 11). While decision trees are less accurate than Random Forest models, they offer

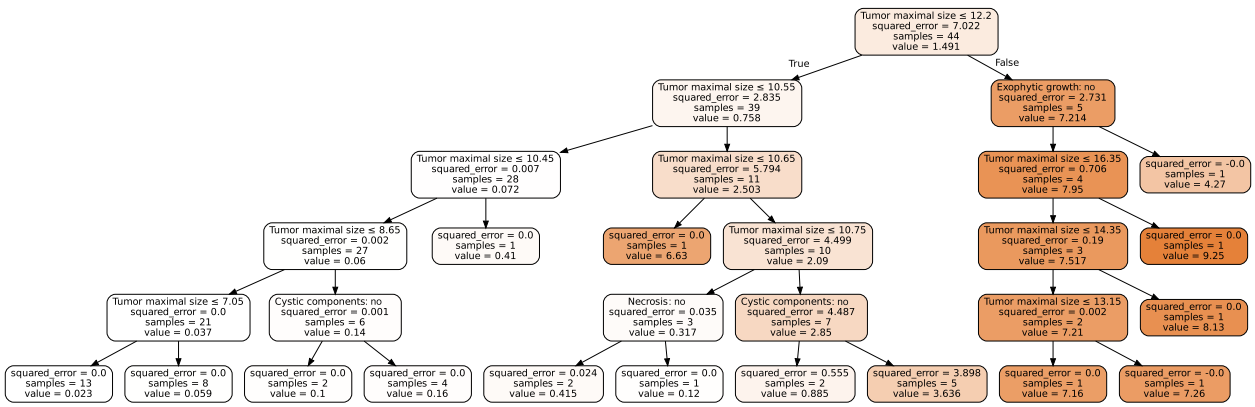

Fig. 11 Decision tree for Step 1

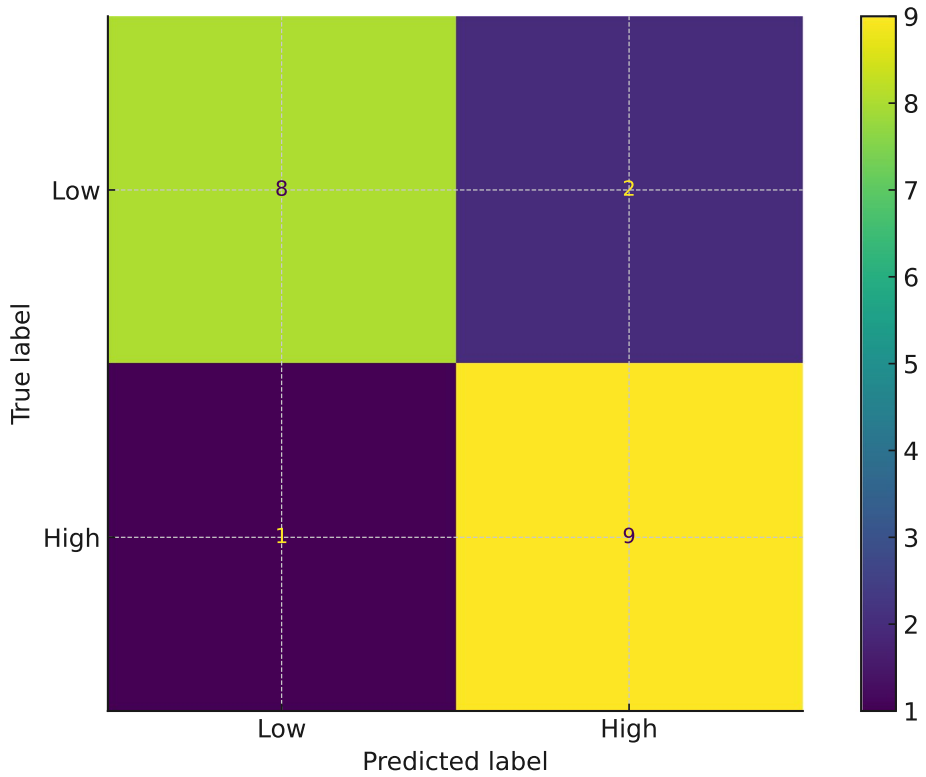

Fig. 12 Confusion matrix for Step 1

valuable insights into the decision-making process of the regression model.

Additionally, for interpretative purposes, the regression outputs were converted into binary classifications using a threshold of ≤0.10 RU to create a confusion matrix (Fig. 12). This allowed an evaluation of the regression model's ability to approximate classification outcomes. However, this approach was auxiliary and aimed at offering additional interpretability, as Step 1 primarily focuses on predicting miR-15a expression as a continuous variable.

Step 2: classifying low vs. high miR-15a expression

A logistic regression model and a Random Forest classifier were employed to classify miR-15a expression as "Low" (≤0.10 RU) or "High" (>0.10 RU). Both models included tumor size and radiological features as predictors.

Variable importance analysis in both approaches consistently highlighted nodular enhancement as the most significant predictor, reaffirming its central role in distinguishing low and high expression levels. Necrosis and tumor size followed as important contributors, while features like cystic components, macroscopic fat, and exophytic growth had lower contributions (Fig. 13).

The Random Forest model provided additional interpretability by highlighting non-linear contributions of tumor size and interactions with other features, complementing the logistic regression findings (Fig. 14). The classification models achieved exceptional performance, with the logistic regression model achieving a precision of 1.0, recall of 0.9, and an F1-score of 0.947.

A decision tree classifier was constructed to visualize the feature splits for classifying low vs. high miR-15a expression. The tree highlighted key decision points, such as thresholds for nodular enhancement and necrosis, which aligned with their importance in distinguishing between expression levels. This graphical representation provided an accessible means of interpreting the classification model's decision-making process (Fig. 15).

The ROC analysis demonstrated perfect discrimination (AUC = 1.0), showcasing the model's ability to differentiate between low and high miR-15a expression levels effectively.

The confusion matrix further supported these findings, showing only one false negative, with all other predictions being correct (Fig. 16). This performance underscores the robustness of the classification models and the central role of vascular and tumor-related radiological features in stratifying miR-15a expression levels, Table 4.

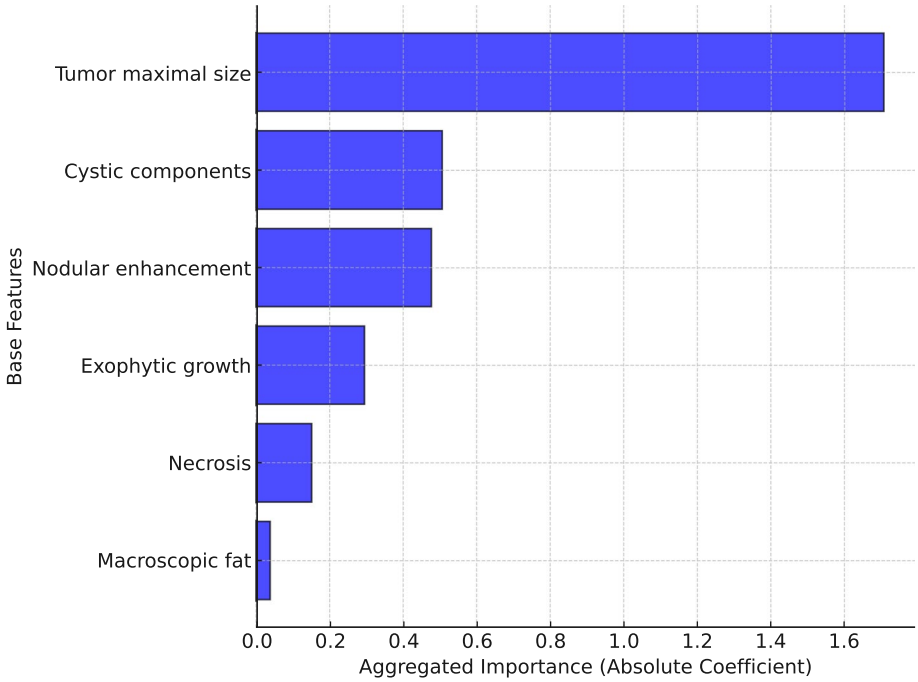

Fig. 13 Variable importance analysis for Step 2

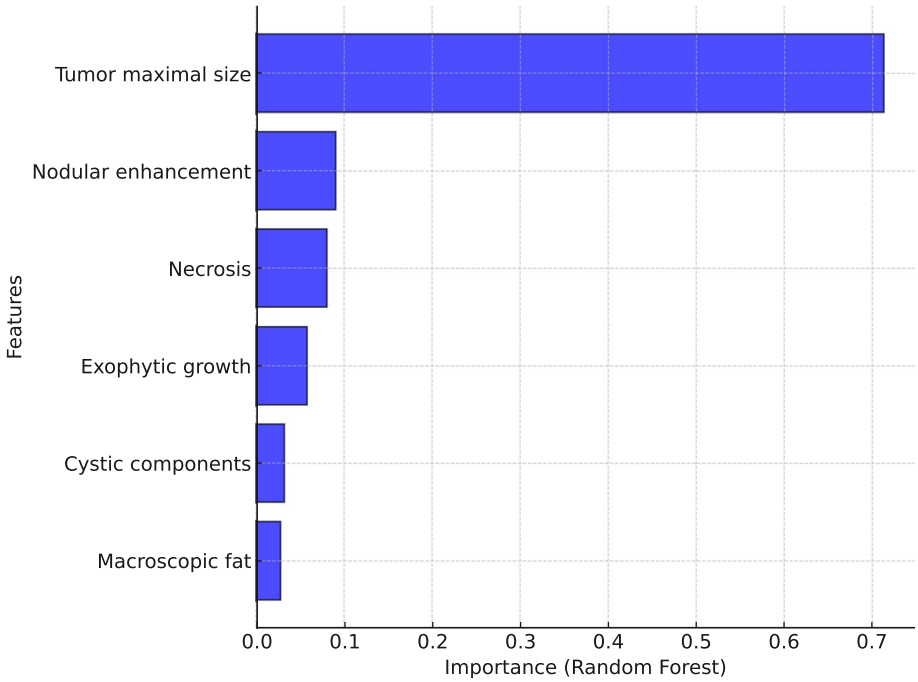

Fig. 14 Random forest model for Step 2

The 3D scatter plot was used to illustrate the spatial distribution of patients based on PCA derived from key radiological features—tumor size, cystic components, and nodular enhancement. Using K-means clustering, the data were separated into two distinct groups, reflecting inherent patterns in the radiological characteristics of

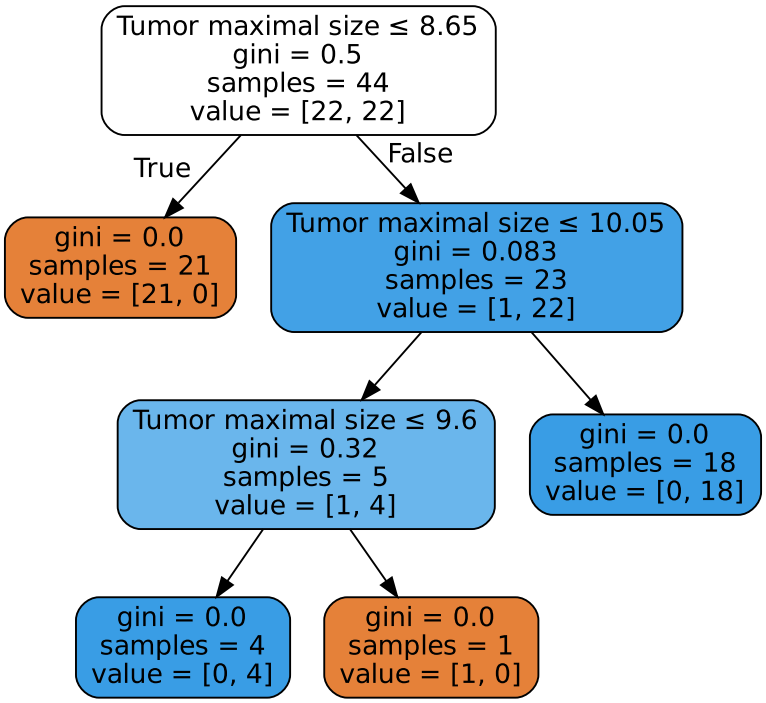

Fig. 15 Decision tree for Step 2

renal tumors. The clusters were found to be visually well-separated, suggesting a strong association between radiological phenotypes and underlying tumor biology. One cluster was observed to likely represent tumors with less aggressive features (e.g., smaller size, presence of cystic components, absence of nodular enhancement), which are correlated with lower miR-15a expression levels. In contrast, the other cluster appeared to include tumors with more aggressive radiological features (e.g., larger size, nodular enhancement), associated with higher miR-15a expression (Fig. 17).

Discussion

Radiogenomics, which integrates imaging phenotypes with genomic data, has emerged as a crucial tool in oncology [37, 41, 42]. This study highlights the potential of radiogenomic analysis for predicting miR-15a expression in RCC, demonstrating robust performance and advancing non-invasive approaches to tumor stratification.

miR-15a has emerged as a significant prognostic marker in RCC, with elevated levels associated with higher tumor grades, reduced overall survival, and resistance to apoptosis. These effects are linked to its modulation of key oncogenic pathways, including the Phosphoinositide 3-Kinase/Protein Kinase B/Mechanistic Target of Rapamycin (PI3K/Akt/mTOR) pathway, vascular endothelial growth factor-mediated angiogenesis, and the BCL2-regulated apoptotic pathway [8, 11, 19, 23, 25]. Our previous research demonstrated poorer survival rates in patients with high miR-15a tissue expression, highlighting its potential for enhancing RCC risk stratification [31, 34].

The analysis revealed significant variations in miR-15a expression across radiologic RCC features. High miR-15a expression in tumors with necrosis suggests its involvement in pathways associated with tumor progression and metastasis, consistent with previous findings highlighting the role of miRNA regulation in aggressive RCC phenotypes [23, 25, 31]. Similarly, the correlation between nodular enhancement and elevated miR-15a expression reinforces its prognostic significance, as vascular patterns often reflect tumor angiogenesis and invasion [25, 33].

Nodular enhancement was the most influential feature in our predictive models, with tumors exhibiting nodular enhancement showing significantly higher miR-15a expression (2.91 ± 3.24 RU) compared to those without (0.68 ± 1.72 RU, $p < 0.05$). This finding aligns with Bowen et al., who demonstrated that vascular patterns, including nodular enhancement, are strongly associated with aggressive RCC subtypes [43]. Our model's feature importance analysis identified nodular enhancement as the top predictor, reinforcing its relevance for tumor aggressiveness and angiogenesis.

Our findings confirm necrosis as a significant predictor of high miR-15a expression, with tumors showing necrosis demonstrating a mean expression of 3.45 ± 3.19 RU, significantly higher than tumors without necrosis

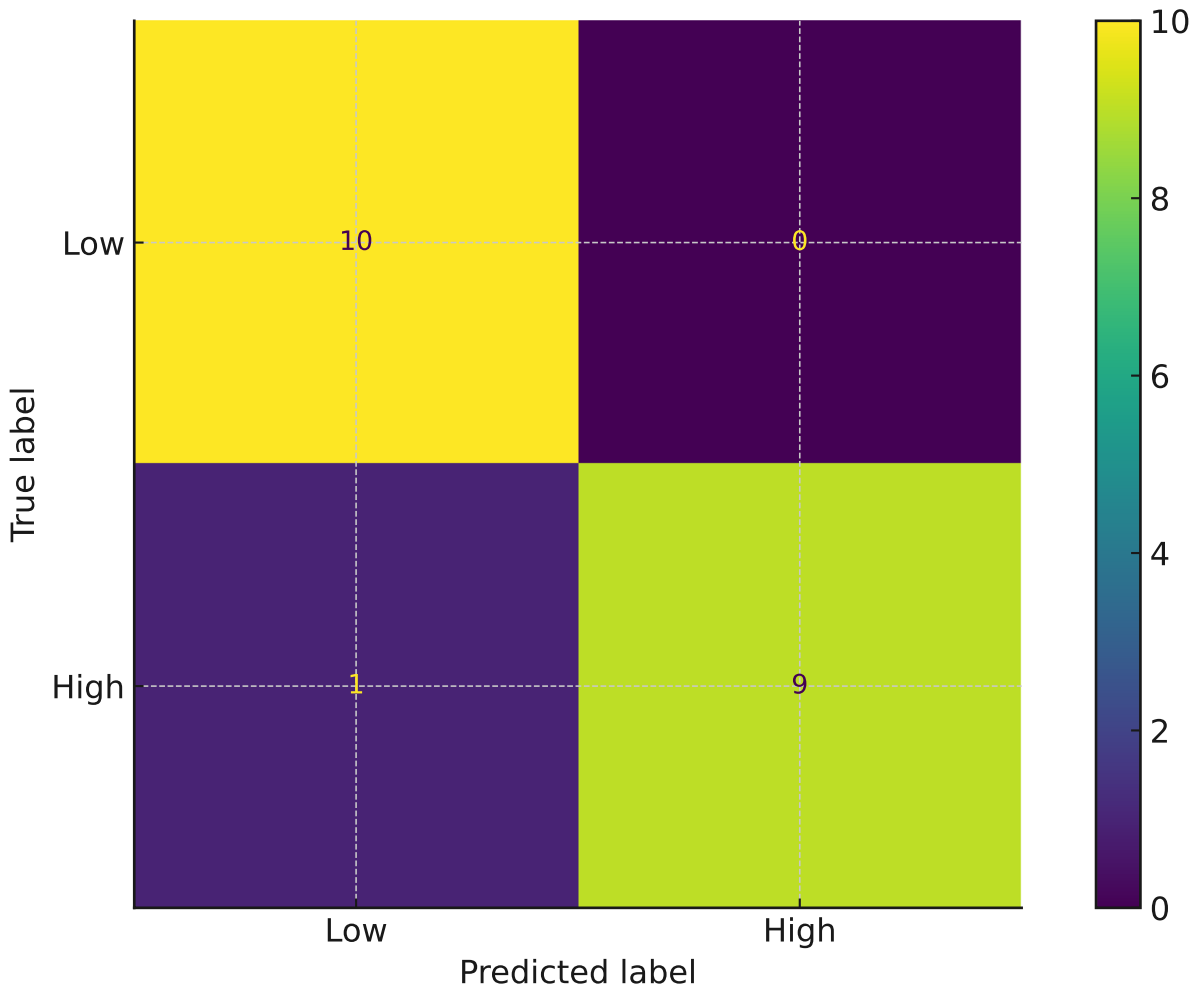

Fig. 16 Confusion matrix for Step 2

Table 4 Confusion matrix results with metrics for Steps 1 and 2

Step	True Negatives	False Positives	False Negatives	True Positives	Accuracy	Precision	Recall	F1-Score
Step 1	8	2	1	9	0.85	0.82	0.90	0.86
Step 2	10	0	1	9	0.95	1.0	0.90	0.95

(0.57 ± 1.63 RU, $p < 0.05$). These results align with Mariglianoet al., where entropy-related features from CT imaging showed strong correlations with miR expression in aggressive RCC phenotypes [40]. Our study further demonstrates the value of heterogeneity metrics such as skewness and kurtosis, which underscore the biological complexity of necrotic regions.

Conversely, tumors with macroscopic fat exhibited the lowest miR-15a expression in our study (0.30 ± 0.87 RU, compared to 1.83 ± 2.83 RU in fat-free tumors, $p < 0.05$). This supports findings by Greco et al., which linked fat-containing tumors to lower aggressiveness based on radiogenomic lipid metabolism signatures [41]. These results collectively emphasize that macroscopic fat is a key marker of less aggressive tumor phenotypes. Additionally, the low miR-15a levels associated with cystic components and exophytic growth further underscore its potential in differentiating indolent from aggressive lesions, thereby contributing to personalized treatment planning.

Hierarchical clustering in our study effectively stratified tumors into aggressive and indolent phenotypes.

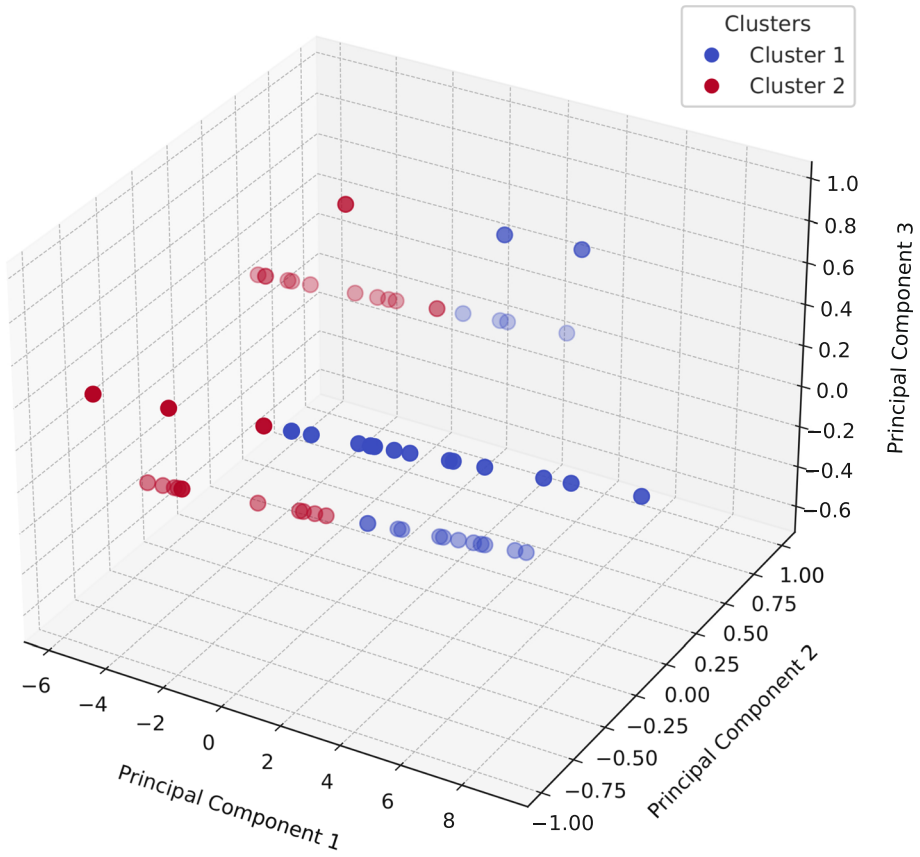

Fig. 17 3D scatter plot of radiological features, including tumor size, with K-means clustering

Tumors with necrosis and nodular enhancement clustered together with larger tumor sizes, while those with cystic components and macroscopic fat formed distinct clusters linked to lower miR-15a expression. This clustering approach mirrors the findings of Bowen et al. [43], where radiogenomic subtyping revealed similar clustering patterns for aggressive versus indolent RCC phenotypes.

Machine learning models in this study demonstrated strong predictive performance for miR-15a expression using radiological features. Regression and classification models consistently highlighted the importance of nodular enhancement, necrosis, and tumor size in predicting miR-15a expression and stratifying patients into expression groups. This aligns with findings from Khaleel et al., where radiogenomic studies showed that integrating radiological features with genomic data enhanced predictions of molecular and clinical outcomes in ccRCC [36]. Similarly, radiomics and machine learning approaches have been effectively used to assess gene expression and mutational status, further supporting the inclusion of comprehensive radiological data in predictive modeling [42].

Despite initial lack of standalone statistical significance, the inclusion of radiological features in the polynomial regression model significantly improved its predictive accuracy for miR-15a expression. Tumor size alone accounted for 82.81% of the variance in miR-15a expression (adjusted $R^2 = 0.8281$, $p < 0.001$). However, integrating features such as nodular enhancement, necrosis, exophytic growth, and cystic components further enhanced model performance (adjusted $R^2 = 0.8336$, $p < 0.001$). Notably, Marigliano et al. found that combining texture features from CT images with miRNA expression data provided valuable non-invasive insights for cancer characterization [40].

Machine learning validation underscored the predictive contributions of radiological features, even when they lacked significance in isolation. The Random Forest model emphasized the dominant role of nodular enhancement, occasionally surpassing tumor size in predictive strength. These findings are consistent with insights from advanced radiogenomic studies, such as those by Sindhu et al., where incorporating radiological features into predictive models enhanced precision and revealed non-linear interactions [6]. These results

highlight the critical importance of multifactorial and non-linear analyses in radiogenomic models.

Our Random Forest regression model achieved an R^2 of 0.658, explaining 65.8% of the variance in miR-15a expression, with a RMSE of 1.454 RU. In classifying low and high miR-15a expression, our model achieved an AUC of 1.0, demonstrating perfect discrimination. The inclusion of a healthy control group was not found to improve model performance, as R^2 significantly decreased, likely due to the absence of imaging data in healthy controls. This resulted in bias and increased model variance, confirming that control samples did not enhance predictive capability. Consequently, they were excluded from the final model. These results surpass the performance of models discussed in Wang et al., where a multi-modal approach combining radiomics, deep learning (DL), and transcriptomics achieved an AUC of 0.864 for pathological grade prediction [42]. Our model, relying solely on radiological features, provides comparable accuracy, highlighting its practical utility in resource-limited clinical settings.

Our model's reliance on readily available radiological features, coupled with its high predictive accuracy (AUC = 1.0, F1-score = 0.95), underscores its clinical applicability. Unlike multi-modal approaches requiring genomic data, our method offers a cost-effective solution for non-invasive miR-15a prediction, suitable for diverse healthcare settings.

The findings from K-means clustering, applied to radiological features including tumor size and utilizing PCA, supported the hypothesis that radiological features serve as reliable non-invasive predictors of miR-15a expression. This approach provides valuable insights for patient stratification and personalized management in RCC. Moreover, the distinct separation between clusters underscores the potential of machine learning to identify complex, clinically relevant patterns within radiogenomic datasets.

By leveraging machine learning, this study demonstrates the potential to uncover complex predictive relationships, advancing the integration of imaging and molecular data in cancer prognosis and personalized treatment strategies. Furthermore, the scalability of machine learning algorithms enables the application of our model across diverse patient populations and imaging modalities. Unlike traditional models, which may rely on invasive tissue biopsies or limited clinical data, our approach provides a cost-effective and non-invasive solution for miRNA-based risk stratification. This advancement is particularly relevant in resource-limited settings, where access to genomic testing is often restricted. Future efforts should focus on validating these models in larger datasets and integrating them into clinical workflows for RCC management.

Although our primary goal was to develop a radiogenomic model for miR-15a prediction, we recognized that necrosis, linked to more aggressive tumor behavior and poorer outcomes [44], could confound the strong relationship between tumor size and miR-15a. Consequently, we conducted additional linear regressions (Supplementary Table S1) to determine whether necrosis independently affected miR-15a once tumor size was accounted for. The analysis demonstrated that necrosis was not a confounding factor, suggesting that the observed association between tumor size and miR-15a expression remained robust regardless of necrosis status.

This study has several limitations. First, the focus on qualitative imaging features may limit the model's predictive strength and applicability; future work should include quantitative metrics like radiomic texture and shape. Second, the analysis was restricted to ccRCC. Third, the lack of external validation limits generalizability. Finally, the retrospective design introduces potential selection bias.

Conclusion

This study highlights the potential of machine learning-assisted radiogenomic analysis in predicting miR-15a expression in RCC. By linking radiological features with molecular markers, it offers a non-invasive tool for tumor stratification and personalized management. The findings underscore the prognostic value of miR-15a and its association with key radiological features, paving the way for integrating radiogenomics into clinical practice. Future research should focus on validating these results, exploring additional imaging metrics, and uncovering the biological mechanisms driving miR-15a expression, advancing precision medicine and improving outcomes for RCC patients.

Abbreviations

AJCC	American Joint Committee on Cancer
AUC	Area Under the Curve
CMP	Corticomedullary Phase
DL	Deep Learning
EP	Excretory Phase
ET-1	Endothelin-1
FFPE	Formalin-Fixed Paraffin-Embedded
FOV	Field of View
FSPGR	Fast Spoiled Gradient-Recalled-Echo
ISUP	International Society of Urological Pathology
LAVA	Liver Acquisition with Volume Acceleration
MCECT	Multiphase Contrast-Enhanced Computed Tomography
MIP	Maximum Intensity Projection
MRI	Magnetic Resonance Imaging
MSE	Mean Squared Error
NCP	Non-Contrast Phase
NEX	Number of Excitations
NF-κB	Nuclear Factor Kappa B
NP	Nephrographic Phase
PI3K/AKT/mTOR	Phosphoinositide 3-Kinase/Protein Kinase B/Mechanistic Target of Rapamycin

PKCα	Protein Kinase C Alpha
RCC	Renal Cell Carcinoma
RMSE	Root Mean Square Error
ROC	Receiver Operating Characteristic
RU	Relative Units
SNR	Signal-to-Noise Ratio
T1W	T1-Weighted
T2W	T2-Weighted
TE	Echo Time
TNM	Tumor, Node, Metastasis Classification System
TR	Repetition Time
miR-15a	MicroRNA-15a
qPCR	Quantitative Polymerase Chain Reaction

Supplementary Information

The online version contains supplementary material available at https://doi.org/10.1186/s12885-025-13963-x.

Supplementary Material 1.

Acknowledgements
Not applicable.

Authors' contributions
YM conceived the conception and design of the study, performed acquisition of data, data analysis and interpretation, paper preparation, final approval. PK conceived the conception and design of the study. YK performed acquisition of data, drafting the article. ML performed literature research. MS performed data analysis and interpretation. DS performed statistic data analysis. VD performed molecular data acquisition. OK performed literature research. All authors reviewed the manuscript.

Funding
The authors declare that no funds, grants, or other support were received during the preparation of this manuscript.

Data availability
The datasets used and analyzed during the current study available from the corresponding author on reasonable request.

Declarations

Ethics approval and consent to participate
This retrospective study received approval from the Bioethical Committee of Danylo Halytsky Lviv National Medical University (protocol #5, dated 25.05.2015). All procedures were conducted in accordance with the ethical guidelines established by institutional and national research committees, adhering to the principles of the 1964 Helsinki Declaration and its later amendments or equivalent ethical standards. The study was carried out between 2015 and 2024. For inclusion in the study, all patients signed written informed consent forms.

Consent for publication
Not applicable.

Competing interests
The authors declare no competing interests.

Author details
[1]Voxel Medical Diagnostic Centers, Katowice, Poland. [2]Department of Urology, Danylo Halytsky Lviv National Medical University, Lviv, Ukraine. [3]Department of Urology, Regional Specialist Hospital, Wroclaw, Poland. [4]Department of Urology, St. Padre Pio Regional Hospital in Przemysl, Przemysl, Poland. [5]Department of Urology, Centre of Postgraduate Medical Education, Independent Public Hospital of Prof. W. Orlowski, Warsaw, Poland. [6]Department of General and Molecular Pathophysiology, Bogomoletz Institute of Physiology of National Academy of Sciences of Ukraine, Kiev, Ukraine. [7]Visio-Med, Kąty Wrocławskie, Poland.

Received: 11 January 2025 Accepted: 18 March 2025
Published online: 20 August 2025

References

1. Sung H, Ferlay J, Siegel RL, Laversanne M, Soerjomataram I, Jemal A, et al. Global Cancer Statistics 2020: GLOBOCAN Estimates of Incidence and Mortality Worldwide for 36 Cancers in 185 Countries. CA Cancer J Clin. 2021;71:209–49.
2. Campbell SC, Clark PE, Chang SS, Karam JA, Souter L, Uzzo RG. Renal Mass and Localized Renal Cancer: Evaluation, Management, and Follow-Up: AUA Guideline: Part I. J Urol. 2021;206:199–208.
3. Fiori C, Porpiglia F. Renal cancer: From current evidence to future perspectives. Asian J Urol. 2022;9:199–200.
4. Gatta R, Depeursinge A, Ratib O, Michielin O, Leimgruber A. Integrating radiomics into holomics for personalised oncology: from algorithms to bedside. European Radiology Experimental. 2020;4:11.
5. Bedke J, Albiges L, Capitanio U, Giles RH, Hora M, Ljungberg B, et al. The 2022 Updated European Association of Urology Guidelines on the Use of Adjuvant Immune Checkpoint Inhibitor Therapy for Renal Cell Carcinoma. Eur Urol. 2023;83:10–4.
6. Sindhu KK, Dovey Z, Thompson M, Nehlsen AD, Skalina KA, Malachowska B, et al. The potential role of precision medicine to alleviate racial disparities in prostate, bladder and renal urological cancer care. BJUI Compass. 2024;5:405–25.
7. Yousef GM. Personalized Medicine in Kidney Cancer: Learning How to Walk Before We Run. Eur Urol. 2015;68:1021–2.
8. Elballal MS, Sallam A-AM, Elesawy AE, Shahin RK, Midan HM, Elrebehy MA, et al. miRNAs as potential game-changers in renal cell carcinoma: Future clinical and medicinal uses. Pathol Res Pract. 2023;245:154439.
9. Li M, Wang Y, Song Y, Bu R, Yin B, Fei X, et al. MicroRNAs in renal cell carcinoma: a systematic review of clinical implications (Review). Oncol Rep. 2015;33:1571–8.
10. Ghafouri-Fard S, Shirvani-Farsani Z, Branicki W, Taheri M. MicroRNA Signature in Renal Cell Carcinoma. Front Oncol. 2020;10:596359.
11. Chakrabortty A, Patton DJ, Smith BF, Agarwal P. miRNAs: Potential as Biomarkers and Therapeutic Targets for Cancer. Genes (Basel). 2023;14:1375.
12. Jiao X, Qian X, Wu L, Li B, Wang Y, Kong X, et al. microRNA: The Impact on Cancer Stemness and Therapeutic Resistance. Cells. 2019;9:8.
13. Gaál Z. Role of microRNAs in Immune Regulation with Translational and Clinical Applications. Int J Mol Sci. 2024;25:1942.
14. Xu P, Wang Y, Deng Z, Tan Z, Pei X. MicroRNA-15a promotes prostate cancer cell ferroptosis by inhibiting GPX4 expression. Oncol Lett. 2022;23:67.
15. Yang J, Xiang H, Cheng M, Jiang X, Chen Y, Zheng L, et al. microRNA-15a-5p suppresses hypoxia-induced tumor growth and chemoresistance in bladder cancer by binding to eIF5A2. Neoplasma. 2024;71:60–9.
16. Zhao X-Q, Tang H, Yang J, Gu X-Y, Wang S-M, Ding Y. MicroRNA-15a-5p down-regulation inhibits cervical cancer by targeting TP53INP1 in vitro. Eur Rev Med Pharmacol Sci. 2019;23:8219–29.
17. Shen R, Wang X, Wang S, Zhu D, Li M. Long Noncoding RNA CERS6-AS1 Accelerates the Proliferation and Migration of Pancreatic Cancer Cells by Sequestering MicroRNA-15a-5p and MicroRNA-6838-5p and Modulating HMGA1. Pancreas. 2021;50:617–24.
18. Utaijaratrasmi P, Vaeteewoottacharn K, Tsunematsu T, Jamjantra P, Wongkham S, Pairojkul C, et al. The microRNA-15a-PAI-2 axis in cholangiocarcinoma-associated fibroblasts promotes migration of cancer cells. Mol Cancer. 2018;17:10.
19. Aqeilan RI, Calin GA, Croce CM. miR-15a and miR-16-1 in cancer: discovery, function and future perspectives. Cell Death Differ. 2009;17:215–20.
20. Terzuoli E, Donnini S, Finetti F, Nesi G, Villari D, Hanaka H, et al. Linking microsomal prostaglandin E Synthase-1/PGE-2 pathway with miR-15a and -186 expression: Novel mechanism of VEGF modulation in prostate cancer. Oncotarget. 2016. https://doi.org/10.18632/oncotarget.10051.
21. Zhu K, He Y, Xia C, Yan J, Hou J, Kong D, et al. MicroRNA-15a Inhibits Proliferation and Induces Apoptosis in CNE1 Nasopharyngeal Carcinoma Cells. Oncol Res. 2016;24:145–51.
22. Shinden Y, Akiyoshi S, Ueo H, Nambara S, Saito T, Komatsu H, et al. Diminished expression of MiR-15a is an independent prognostic marker for breast cancer cases. Anticancer Res. 2015;35:123–7.

23. Li G, Chong T, Xiang X, Yang J, Li H. Downregulation of microRNA-15a suppresses the proliferation and invasion of renal cell carcinoma via direct targeting of eIF4E. Oncol Rep. 2017;38:1995–2002.
24. Li D-Y, Lin F-F, Li G-P, Zeng F-C. Exosomal microRNA-15a from ACHN cells aggravates clear cell renal cell carcinoma via the BTG2/PI3K/AKT axis. Kaohsiung J Med Sci. 2021;37:973–82.
25. Király J, Szabó E, Fodor P, Vass A, Choudhury M, Gesztelyi R, et al. Expression of hsa-miRNA-15b, -99b, -181a and Their Relationship to Angiogenesis in Renal Cell Carcinoma. Biomedicines. 2024;12:1441.
26. von Brandenstein M, Depping R, Schäfer E, Dienes H-P, Fries JWU. Protein kinase C α regulates nuclear pri-microRNA 15a release as part of endothelin signaling. Biochim Biophys Acta - Mol Cell Res. 2011;1813:1793–802.
27. Schütte U, Bisht S, Heukamp LC, Kebschull M, Florin A, Haarmann J, et al. Hippo signaling mediates proliferation, invasiveness, and metastatic potential of clear cell renal cell carcinoma. Transl Oncol. 2014;7:309–21.
28. Li T, Morgan MJ, Choksi S, Zhang Y, Kim Y-S, Liu Z. MicroRNAs modulate the noncanonical transcription factor NF-κB pathway by regulating expression of the kinase IKKα during macrophage differentiation. Nat Immunol. 2010;11:799–805.
29. Morais C, Gobe G, Johnson DW, Healy H. The emerging role of nuclear factor kappa B in renal cell carcinoma. Int J Biochem Cell Biol. 2011;43:1537–49.
30. Mytsyk Y, Dosenko V, Borys Y, Kucher A, Gazdikova K, Busselberg D, et al. MicroRNA-15a expression measured in urine samples as a potential biomarker of renal cell carcinoma. Int Urol Nephrol. 2018;50(5):851–9.
31. Mytsyk Y, Borys Y, Tumanovska L, Stroy D, Kucher A, Gazdikova K, et al. MicroRNA-15a tissue expression is a prognostic marker for survival in patients with clear cell renal cell carcinoma. Clin Exp Med. 2019. https://doi.org/10.1007/s10238-019-00574-7.
32. Cimadamore A, Franzese C, Di Loreto C, Blanca A, Lopez-Beltran A, Crestani A, et al. Predictive and prognostic biomarkers in urological Tumors. Pathology. 2024;56:228–38.
33. Yang F, Li H, Li T, Zhao Y, Liu Z, Li X. Prognostic Value of MicroRNA-15a in Human Cancers: A Meta-Analysis and Bioinformatics. Biomed Res Int. 2019;2019:2063823.
34. Mytsyk Y, Dosenko V, Skrzypczyk MA, Borys Y, Diychuk Y, Kucher A, et al. Potential clinical applications of microRNAs as biomarkers for renal cell carcinoma. Cent European J Urol. 2018;71:295–303.
35. Gu L, Li H, Chen L, Ma X, Gao Y, Li X, et al. MicroRNAs as prognostic molecular signatures in renal cell carcinoma: a systematic review and meta-analysis. Oncotarget. 2015;6:32545–60.
36. Khaleel S, Katims A, Cumarasamy S, Rosenzweig S, Attalla K, Hakimi AA, et al. Radiogenomics in Clear Cell Renal Cell Carcinoma: A Review of the Current Status and Future Directions. Cancers (Basel). 2022;14:2085.
37. O'Sullivan NJ, Kelly ME. Radiomics and Radiogenomics in Pelvic Oncology: Current Applications and Future Directions. Curr Oncol. 2023;30:4936–45.
38. Ferro M, Musi G, Marchioni M, Maggi M, Veccia A, Del Giudice F, et al. Radiogenomics in Renal Cancer Management-Current Evidence and Future Prospects. Int J Mol Sci. 2023;24:4615.
39. Smith CP, Czarniecki M, Mehralivand S, Stoyanova R, Choyke PL, Harmon S, et al. Radiomics and radiogenomics of prostate cancer. Abdom Radiol (NY). 2019;44:2021–9.
40. Marigliano C, Badia S, Bellini D, Rengo M, Caruso D, Tito C, et al. Radiogenomics in Clear Cell Renal Cell Carcinoma: Correlations Between Advanced CT Imaging (Texture Analysis) and MicroRNAs Expression. Technol Cancer Res Treat. 2019;18:1533033819878458.
41. Greco F, Panunzio A, Bernetti C, Tafuri A, Beomonte Zobel B, Mallio CA. The Radiogenomic Landscape of Clear Cell Renal Cell Carcinoma: Insights into Lipid Metabolism through Evaluation of ADFP Expression. Diagnostics. 2024;14:1667.
42. Wang S, Zhu C, Jin Y, Yu H, Wu L, Zhang A, et al. A multi-model based on radiogenomics and deep learning techniques associated with histological grade and survival in clear cell renal cell carcinoma. Insights Imaging. 2023;14:207.
43. Bowen L, Xiaojing L. Radiogenomics of Clear Cell Renal Cell Carcinoma: Associations Between mRNA-Based Subtyping and CT Imaging Features. Acad Radiol. 2019;26(5):e32–7 Epub 2018 Jul 29.
44. Beddy P, Genega EM, Ngo L, Hindman N, Wei J, Bullock A, et al. Tumor necrosis on magnetic resonance imaging correlates with aggressive histology and disease progression in clear cell renal cell carcinoma. Clin Genitourin Cancer. 2014;12:55–62.

Publisher's Note